CONFERENCE PRE-PRINT

CONFINEMENT PROPERTY IN THE JT-60SA FIRST OPERATIONAL PHASE

Y. Ohtani

National Institutes for Quantum Science and Technology

Naka/Ibaraki, Japan

Email: ohtani.yoshiaki@qst.go.jp

M. Yoshida, T. Nakano, R. Sano, T. Yokoyama, T. Wakatsuki, S, Inoue, H. Urano National Institutes for Quantum Science and Technology Naka/Ibaraki, Japan

Abstract

Characteristics of global energy confinement of L-mode diverted hydrogen plasmas with a plasma current $I_{\rm P}$ of 1 MA in the JT-60SA first plasma operation phase has been investigated. The global energy confinement time is estimated to be around 100 - 200 ms from the power balance equation and the decay time after heating power turned off. The global energy confinement time strongly depends on total heating power. At a comparable heating power, $\tau_{\rm E}$ increases with an increase in a line-averaged electron density $\bar{n}_{\rm e}$. The global energy confinement time is compared with the ITERL-96P(th) scaling law, resulting in $\tau_{\rm E}$ being on and a little below the scaling. Although the global energy confinement time saturates at $\bar{n}_{\rm e} \sim 4 \times 10^{18}$ m⁻³ in the lower-power ohmic heating case, it does not saturate in the higher-power ohmic heating and ECH heating cases. A steeper electron temperature gradient is observed with increasing heating power, which may imply that the dominant turbulent instability remains as trapped electron modes even at high densities.

1. INTRODUCTION

Investigation of the confinement property in a newly developed large tokamak device is an essential issue for improving the extrapolability of results toward ITER and future DEMO reactors. JT-60SA, currently the largest superconducting tokamak, features a toroidal magnetic field $B_{\rm T}$ of 2.25 T, a major radius R of approximately 3 m, and a minor radius a of approximately 1.2 m. The device has successfully achieved its first plasma operation and a plasma current $I_{\rm D}$ of 1.2 MA [1].

Empirical L-mode scalings, such as ITERL-96P(th) scaling [2], typically include explicit size-dependent terms of R, a, and an ellipticity. These relations are derived from existing datasets, and their extrapolation to reactor-scale conditions remains a critical issue. Although plasma density is generally considered to have a weak influence on global energy confinement, an increase in confinement time with increasing density has been observed in relatively low-density plasmas, such as those generated in the first operation phase of JT-60SA [3]. The confinement scaling in this region agrees with the neo-Alcator scaling and reaches the L-mode scaling as the density increases [4]. It is also known that local heating by electron cyclotron resonance heating (ECH), which peaks the electron temperature profile, causes the onset of saturation to occur at a higher density because the dominant turbulent instability remains as trapped electron modes even at high densities [5]. As the density increases, this linear dependence transitions to a regime where the confinement time becomes less sensitive to density. Such a transition in density dependence may become relevant in interpreting the confinement behavior observed in JT-60SA plasmas.

In the first operational phase, only limited diagnostics were available [6]. Nevertheless, a systematic study of the global energy confinement characteristics was conducted for hydrogen (H) plasmas at $I_{\rm p}=1$ MA. The confinement time $\tau_{\rm E}$ was evaluated from the energy balance, and its dependence and comparison with the existing scalings were investigated.

2. EXPERIMENTAL SETUP AND RESULTS

For all discharges analyzed in this study (E101160, E101162, and E101163), the toroidal magnetic field was fixed at 2.0 T, and the plasma was configured in an upper single-null geometry. Plasma-facing components included an

upper divertor and inner first wall made of carbon, and outer limiters made of stainless steel. Wall conditioning was performed by baking the vacuum vessel up to 200 °C and by glow discharge cleaning. The 110 GHz ECH (the second-harmonic X-mode EC wave) was used as the auxiliary heating system during the analysis windows [7]. The line-integrated electron density n_eL was measured using a two-color CO_2 laser interferometer along a tangential chord [8, 9]. Although this interferometer had the tangential chord, it was designed to pass close to the inner wall, so that the path length in the peripheral region was slightly longer but essentially uniform. The electron temperature $T_{\rm e}$ was obtained from a double-filter soft X-ray (SX) system with 7 μ m and 50 μ m filters, the 16 chords of which covered the core to edge regions [10]. Although the electron density $n_{\rm e}$ profile was not available, T_e profile was able to be evaluated from the ratio of soft X-ray (SX) emission profiles obtained by detectors equipped with 7 μ m and 50 μ m filters. These SX emission profiles were reconstructed using Tikhonov– Philips regularization. The magnetic flux surfaces were calculated using the SELENE MHD equilibrium code, which was employed both for determining the interferometer path length and reconstructing the SX radial profile [11]. Visible spectroscopy measured the $H\alpha$ line emission along the same tangential chord as the interferometer. Stored energy $W_{\rm st}$ was obtained from diamagnetic measurements [12]. Due to the limitations of diagnostics, quantities such as impurity content were not evaluated.

The engineering and operational parameters are summarized in Table 1. While the plasma size and shape are nearly constant, the line-averaged electron density \bar{n}_e , T_e at normalized minor radius $\rho = 0.1$, and $W_{\rm st}$ are varied by adjusting the gas flow rate GP and ECH injection power $P_{\text{ECH}}^{\text{inj}}$. Here, ρ is defined as $\rho(R,Z) = (\Psi(R,Z) - \Psi(R,Z))$ Ψ_0)/ $(\Psi_{\rm fs} - \Psi_0)$, where $\Psi(R, Z)$, Ψ_0 , and $\Psi_{\rm fs}$ are poloidal magnetic flux at (R, Z), the minimum value of Ψ , and Ψ at magnetic flux surface, respectively. The safety factor q_{95} is evaluated from the empirical equations as

$$q_{95} = q \frac{1 + \kappa^2 (1 + 2\delta^2 - 1.2\delta^3)}{2} \frac{1.17 - 0.65\epsilon}{(1 - \epsilon^2)^2}, \tag{1}$$

$$q_{95} = q \frac{1 + \kappa^2 (1 + 2\delta^2 - 1.2\delta^3)}{2} \frac{1.17 - 0.65\epsilon}{(1 - \epsilon^2)^2},$$

$$q = \frac{5a^2 B_{\rm T}}{RI_{\rm p}},$$
(1)

where δ , κ , and ϵ are the triangularity at the separatrix, the ellipticity at the separatrix, and the inverse aspect ratio of a/R, respectively [13].

The time traces of the H plasma are shown in Fig. 1. The plasma start-up is assisted by 82 GHz ECH (the fundamental O-mode EC wave) and 110 GHz ECH. After I_D reaches 0.5 MA, the plasma configuration changes from a limiter configuration to a divertor configuration. Simultaneously, $H\alpha$ emission intensity decreases as shown in Fig. 1(b). Then, I_p increases up to 1 MA. In this discharge, the ECH was switched off, and a decrease in the core temperature ($T_e(0.1)$: T_e at $\rho = 0.1$) is observed in Fig. 1(c). Here, T_e^{SXch11} in this figure is T_e estimated from the central chord of the SX measurement (ch 11). Only the prefill gas is used in this discharge, whereas in the other discharges, \bar{n}_e is varied by changing the gas flow rate. At the timing of ECH switching off, $W_{\rm st}$ decreases is also observed, the variation of which is qualitatively consistent with the behavior of \bar{n}_e and $T_e(0.1)$.

The operation regime of \bar{n}_e and $T_e(0.1)$ in the target discharges is summarized in Fig. 2(a). The line-averaged electron density \bar{n}_e achieves $\sim 6.5 \times 10^{18}~\text{m}^{-3}$ by the H_2 gas injection of 8.8 $\times 10^{20}~\text{s}^{-1}$ at maximum, where the Greenwald fraction $f_{\rm GW}$ is ~ 0.3 . Although the discharges analyzed in this study are in a quite low-density regime, helium plasmas reaching near $f_{\rm GW}\sim 1$ are achieved at 500 kA [14]. Due to the coil voltage limitation in the first operation phase, a slow ramp-up of $I_{\rm p}$ was required. Additionally, due to the limited operational time of the ECH system, the plasma had to be maintained without auxiliary heating. As a result, an edge cooling due to gas fueling could reach the rational surface, triggering MHD instabilities and leading to radiative disruptions [15]. To avoid this instability, the fueling rate had to be significantly restricted, which consequently prevented the achievement of high density in the 1 MA discharge. The core $T_{\rm e}$ reaches 1.8 keV during ECH injection (t = 5.0s in Fig. 1), then decreases to 1.3 keV after ECH is turned off (t = 5.5 s in Fig. 1), where \bar{n}_e is approximately constant of $4 \times 10^{18} \text{ m}^{-3}$. In Fig. 2(b), the change of $T_{\rm e}$ profile and the ECH deposition profile are shown. The beam power deposition is concentrated on $\rho \approx 0.1$, where the EC beam intersects the resonance layer of the 110 GHz wave, leading to a rise of $T_{\rm e}$ in the core region while having negligible effect on the edge region. Here, the beam power deposition and the absorption power $P_{\rm ECH}^{\rm abs}$ are evaluated under the assumption of a cold plasma approximation. The beam trajectory of the EC wave is evaluated by a quasi-optical beam tracing code, PARADE [16]. Because the electron density $n_{\rm e}$ profile is required in this calculation, the shape of $n_{\rm e}$ profile is fixed by assuming $n_{\rm e} = n_{\rm e0} \left[0.9(1 - \rho^{16}) + 0.1 \right]$, where $n_{\rm e0}$ is the density at $\rho = 0$. Because approximately 80–90% of the injection power is absorbed in the single-pass trajectory, absorption due to multiple reflections at the wall is not taken into account.

TABLE 1. Engineering parameters and operational parameters.

Engineering Parameter	Value	Operational parameter	Value
\overline{R}	3.07 – 3.09 m	$I_{ m p}$	1 MA
a	1.26 – 1.28 m	$W_{ m st}$	66 – 225 kJ
$B_{ m T}$	2.0 T	P_{OH}	0.48 – 0.82 MW
$P_{ m ECH}^{ m inj}$	0 or 0.49 MW	$P_{ m ECH}^{ m abs}$	0 or 0.40 – 0.45 MW (82 – 92%)
\widetilde{GP}^{n}	$0 - 8.8 \times 10^{20} \text{ s}^{-1} / \text{s}$	$\bar{n}_{ m e}^{2011}$	$2.5 - 6.5 \times 10^{18} \text{ m}^{-3}$
		$T_{\rm e}(ho = 0.1)$	0.8 – 1.8 keV
		δ	0.38 - 0.41
		κ	1.49 – 1.53
		q_{95}	13.1 – 13.6

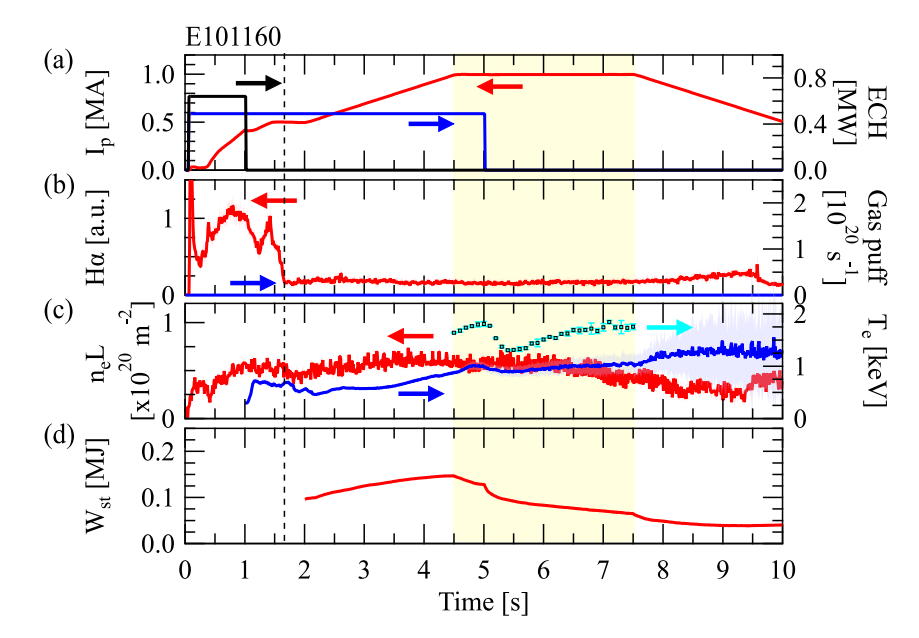


FIG. 1. Example of the time evolution of the H plasma discharge. (a) $I_{\rm p}$ (red), $P_{\rm ECH}^{inj}$ of 82 GHz (black) and $P_{\rm ECH}^{inj}$ of 110 GHz (blue), (b) H_{α} emission (red) and gas flow rate (blue) (c) $n_{\rm e}L$ (red), $T_{\rm e}^{SXch11}$ (blue), and $T_{\rm e}(0.1)$ (cyan) (d) $W_{\rm st}$. The analysis time window is shown as the yellow hatched area. In this experiment, only prefilled gas is injected before t=0 s. The black dotted line indicates when the plasma configuration changed from limiter to divertor.

3. ENERGY CONFINEMENT EVALUATION

The global energy confinement time $\tau_{\rm E}$ of the plasma is evaluated based on the energy balance equation as follows,

$$\tau_{\rm E} = \frac{W_{\rm st}}{P_{\rm OH} + P_{\rm aux} - \frac{dW_{\rm st}}{dt}},\tag{3}$$

where $P_{\rm OH}$ and $P_{\rm aux}$ are the power of the ohmic heating and the auxiliary heating, respectively. The ohmic heating power is evaluated from the loop voltage and $I_{\rm p}$. In the first operation phase, since the auxiliary heating system is only the ECH, $P_{\rm aux}$ equals $P_{\rm ECH}^{\rm abs}$. Figure 3 shows the time evolution of $P_{\rm OH}$, $P_{\rm ECH}^{\rm abs}$, $W_{\rm st}$, and $\tau_{\rm E}$ evaluated by Eq. 3. When the ECH is turned off, $W_{\rm st}$ decreases; however, since the total heating power also drops, $\tau_{\rm E}$ increases. Although $P_{\rm OH}$ decreases with time, $W_{\rm st}$ decreases simultaneously, so $\tau_{\rm E}$ remains nearly constant at about 0.13 s. The decay time after turning off the ECH is also plotted in the figure. It is obtained as the time constant of an exponential fit applied to the period from t=5.025 to t=5

To investigate the dependence of $\tau_{\rm E}$ on the other plasma parameter, $\tau_{\rm E}$ dependence on $P_{\rm total}$ and $\bar{n}_{\rm e}$, which are scanned in the experiments and are also included in the scaling, is investigated. Here, $P_{\rm total}$ is the sum of $P_{\rm ECH}^{\rm abs}$ and $P_{\rm OH}$. In Fig. 4 (a), showing the relationships between $\tau_{\rm E}$ and $P_{\rm total}$, $\tau_{\rm E}$ tends to decrease with increasing $P_{\rm total}$, which is a commonly observed in L-mode plasmas. At comparable heating power levels, however, $\tau_{\rm E}$

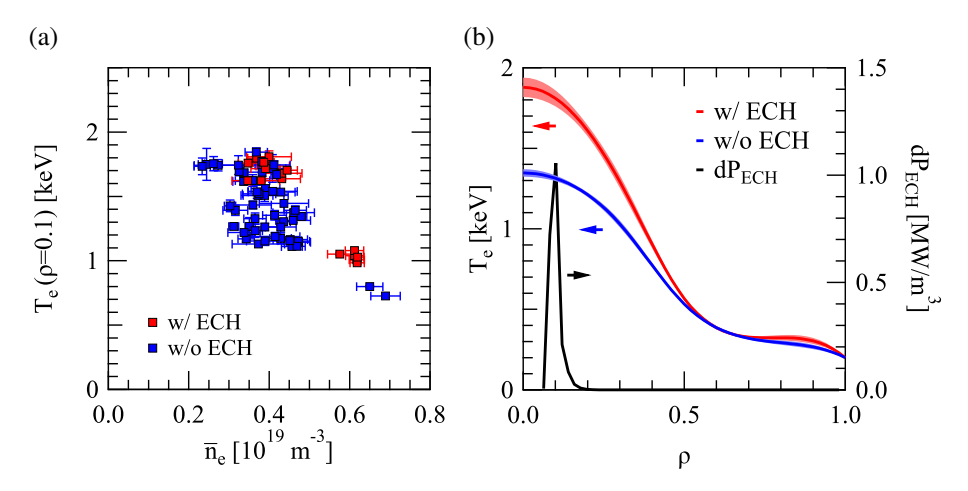


FIG. 2. (a) Operational regime of \bar{n}_e and $T_e(\rho=0.1)$ [14]. (b) T_e profiles with ECH (red) and without ECH (blue), and the power deposition profile of ECH (black).

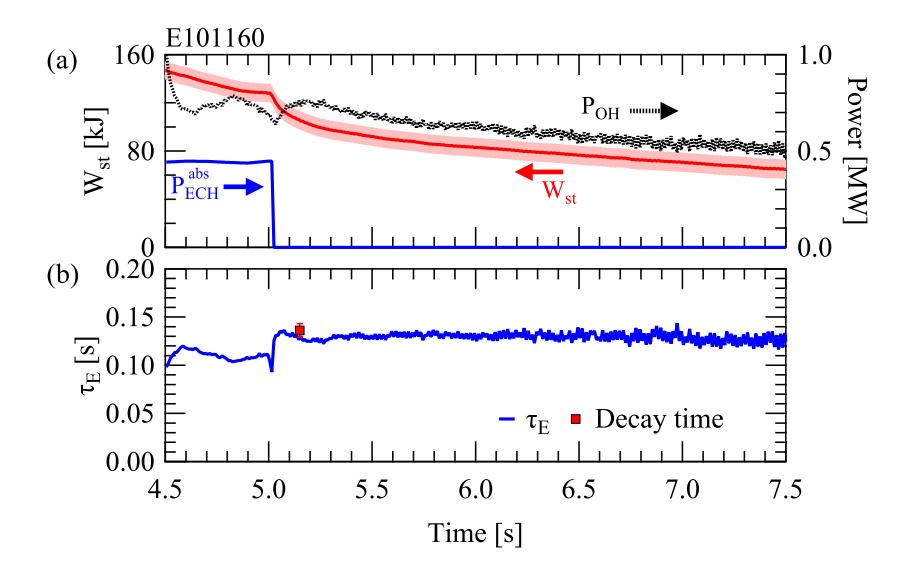


FIG. 3. (a) Time evolution of $W_{\rm st}$ (red), $P_{\rm ECH}^{\rm abs}$ (blue), and $P_{\rm OH}$ (black). (b) Time evolution of $\tau_{\rm E}$ evaluated by Eq. 3 (blue). The red square indicates the decay time of $W_{\rm st}$ between t=5.025-5.3 s.

scatter by approximately a factor of 2. Notably, outliers are found in ohmic plasmas with 0.6–0.8 MW and in ECH plasmas with 1.1–1.4 MW of $P_{\rm total}$. Figure 4(b) shows the relationship between between $\tau_{\rm E}$ and $\bar{n}_{\rm e}$. When $\bar{n}_{\rm e}$ increases, $\tau_{\rm E}$ tends to increase nearly linearly with $\bar{n}_{\rm e}$ and tends to saturate around $\bar{n}_{\rm e}$ of 4×10^{18} m⁻³ in lower $P_{\rm OH}$ case ($P_{\rm total} = 0.4$ –0.6 MW). On the other hand, in higher $P_{\rm OH}$ case (0.6–0.8 MW) and ECH case (1.1–1.4 MW), a linear dependence on $\bar{n}_{\rm e}$ is observed.

4. COMPARISON WITH L-MODE SCALING

To compare $\tau_{\rm E}$ of the JT-60SA plasma in the first operation phase with other devices, the evaluated $\tau_{\rm E}$ is compared with the ITERL-96P(th) scaling as follows,

$$\tau_{\rm E}^{\rm ITERL-96P(th)} = 0.023 I_{\rm p}^{0.96} B_{\rm T}^{0.03} \kappa^{0.96} R^{1.89} a^{-0.06} \bar{n}_{\rm e}^{0.40} M_{\rm eff}^{0.20} P^{-0.73}. \tag{4}$$

Here, $M_{\rm eff}$ and P are the effective atomic mass in atomic mass units, and the estimated total heating power [W] corrected for the time derivative of total plasma energy [J] and for charge exchange and unconfined orbit losses, but not for radiated power [2]. Regarding plasma size, R has a significant impact, whereas a has a negligible influence, and κ exhibits a moderate effect. The data of the ohmic heating plasma may not match the scaling due to the scaling being derived from L-mode discharges with external heating, excluding purely ohmic cases. However, the data from both ohmic and ECH-heated L-mode discharges are overplotted for comparison to assess

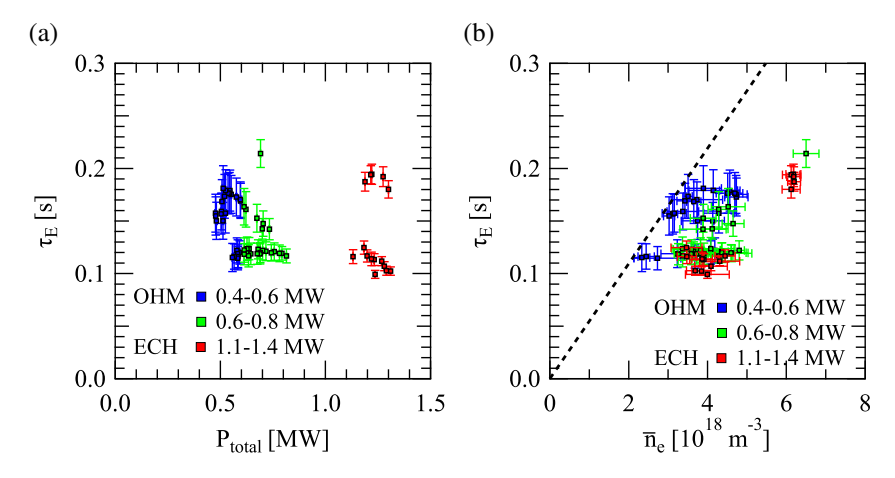


FIG. 4. (a)Relationship between $\tau_{\rm E}$ and $P_{\rm total}$. (b)Relationship between $\tau_{\rm E}$ and $\bar{n}_{\rm e}$. Blue, green, and red squares indicate the cases of $P_{\rm total}$ = 0.4–0.6 MW, $P_{\rm total}$ = 0.6–0.8 MW, and $P_{\rm total}$ = 1.1–1.4 MW, respectively. Black dashed lines indicate the neo-Alcator scaling in this experimental condition.

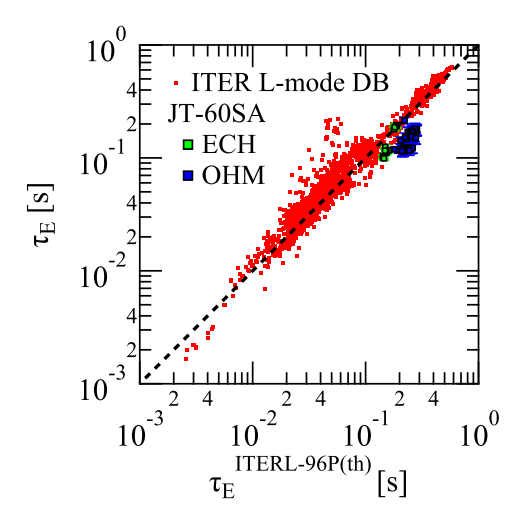


FIG. 5. Comparison of $\tau_{\rm E}$ of JT-60SA with the ITERL-96P(th) scaling. The black dotted line indicates $\tau_{\rm E} = \tau_{\rm E}^{\rm ITERL-96P(th)}$. Red dots indicate the ITER L-mode database version 3.2 (red dots). Green and blue squares indicate the ECH plasma and ohmic plasma in the JT-60SA first operation phase, respectively.

consistency with other devices. This scaling shows that $\tau_{\rm E}$ has a negative dependence on the heating power, which is consistent with the result shown in Fig. 4(a). Although $\tau_{\rm E}$ has a weak dependence on $\bar{n}_{\rm e}$ in this scaling, the result shown in Fig. 4(b) is the more significant $\bar{n}_{\rm e}$ dependence than the scaling. The standard behavior of the energy confinement in the ohmic heating plasma is characterized by a linear increase in $\tau_{\rm E}$ with increasing density referred to as the linear ohmic confinement (LOC) regime - followed by a saturation known as the saturated ohmic confinement (SOC) regime. The neo-Alcator scaling $\tau_{\rm E}^{\rm nA}=0.07\bar{n}_{\rm e}q\sqrt{\kappa a}R^2$, which is used as a comparative reference in ref. [4], explains the experimental data well, suggesting that the ohmic discharges may lie in the LOC regime. Here, the averaged values of q, κ , a and R in the dataset are applied. In particular, in low-power discharges, τ_E appears to saturate around 4×10^{18} m⁻³, indicating a possible transition near the LOC–SOC boundary. In contrast, high-power ohmic and ohmic+ECH-heated plasmas exhibit a linear increase of τ_E with density, extending to higher densities. The detail is discussed in Sec. 5.

In the case of the JT-60SA plasma in the first operation phase, $M_{\rm eff}=1$, and $P=P_{\rm OH}+P_{\rm aux}-dW_{\rm st}/dt$ are applied. Figure 5(a) shows existing L-mode data with additional JT-60SA data plotted on the ITERL-96P(th) scaling. In order to distinguish between ohmic and ECH-heated discharges, the JT-60SA data points are plotted with different colors. In the JT-60SA first operation phase, $\tau_{\rm E}$ of the ECH plasma matches the scaling at higher densities, while it falls below the scaling at lower densities. A similar tendency is also observed in the ohmic plasmas. These results indicate that $\tau_{\rm E}$ of JT-60SA during the first operation phase is well represented by scaling laws established from previous tokamak experiments.

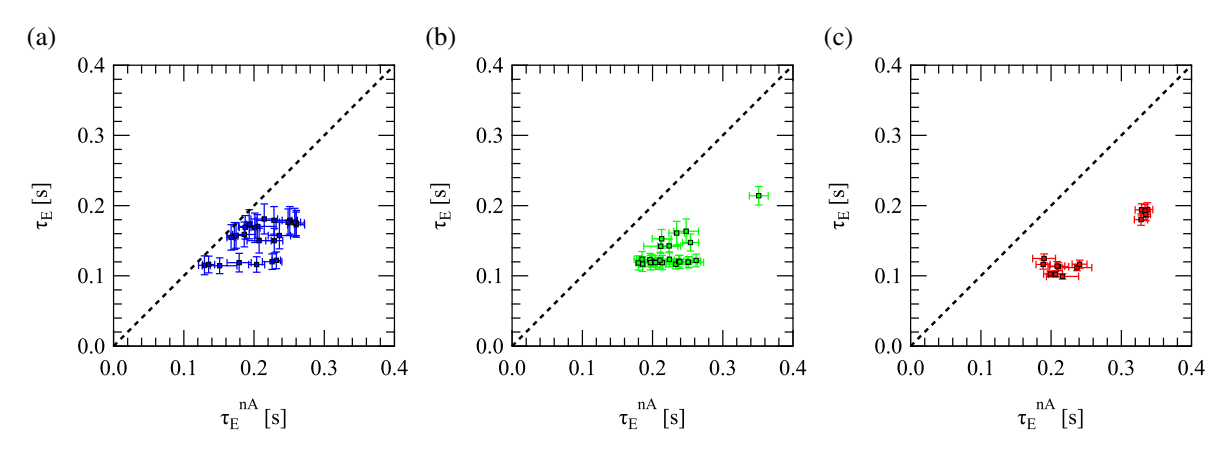


FIG. 6. Comparison of $\tau_{\rm E}$ with the neo-Alcator scaling in the cases of (a) $P_{\rm total} = 0.4$ –0.6 MW, (b) $P_{\rm total} = 0.6$ –0.8 MW, and (c) $P_{\rm total} = 1.1$ –1.4 MW. Black dashed lines indicate $\tau_{\rm E} = \tau_{\rm E}^{nA}$.

5. ENERGY CONFINEMENT TIME DEPENDENCE ON DENSITY

In Sec. 4, a linear dependence of $\tau_{\rm E}$ on $\bar{n}_{\rm e}$ is observed, suggesting that the ohmic discharges may be in the LOC regime. Figure 6 compares the experimental results with the neo-Alcator scaling. To clarify the influence of heating power and to separate ECH-heated discharges, the data are shown in separate panels according to heating power. As has already been described, in the low $P_{\rm total}$ case ($P_{\rm total}=0.4$ -0.6 MW), $\tau_{\rm E}$ follows the neo-Alcator scaling and then saturates. In the higher $P_{\rm total}$ cases, $\tau_{\rm E}$ is lower than the neo-Alcator scaling, and its linear dependence expands to the higher density region than the low $P_{\rm total}$ case. According to Fig. 14 in ref. [4], the product of the critical density $n_{\rm crit}$ for the LOC-SOC transition, q, and R remains within a certain range at a given $B_{\rm T}$. For JT-60SA, where $B_{\rm T}$ is 2 T, a value of $n_{\rm crit}qR$ is in the range of 1.2–1.7 × 10²⁰ m⁻². Thus, the estimated value of $n_{\rm crit}$ is $2.9-4.2\times10^{18}$ m⁻³. This corresponds to τ_E^{RA} in the range of 160–230 ms, where $\tau_{\rm E}$ is saturated in the low $P_{\rm total}$ cases.

In contrast to the low $P_{\rm total}$ cases, plasmas with higher $P_{\rm total}$ and ECH show $\tau_{\rm E}$ is shorter than predicted by the neo-Alcator scaling, and maintains a linear dependence on density in higher \bar{n}_e in this dataset. In ref. [5], it is explained that a large $T_{\rm e}$ gradient due to core ECH injection sustains trapped electron mode (TEM) turbulence, resulting in an extension of the density range where $\tau_{\rm E}$ increases linearly. Figure 7(a) shows that plasmas with similar $\bar{n}_{\rm e}$ exhibit a wide variation in the $T_{\rm e}$ gradient, defined here as $T_{\rm e}(0.1) - T_{\rm e}(0.5)$, within this dataset. Figure 7(b) shows the relation between the $T_{\rm e}$ gradient and $\tau_{\rm E}$. The negative dependence of $\tau_{\rm E}$ on the $T_{\rm e}$ gradient appears, which is qualitatively consistent with the results in ref. [5]. Furthermore, this result indicates that the variation observed at the same density under low heating power conditions can be explained from the aspect of the $T_{
m e}$ gradient. In order to consider the impact of the $T_{\rm e}$ gradient on $\tau_{\rm E}$, the collisionality at $\rho=0.1$ is included because the $T_{\rm e}$ gradient is mainly determined by $T_{\rm e}(0.1)$. Here, the collisionality is defined as $\nu_{\rm eff} \sim 0.1 Z_{\rm eff} n_{\rm e} R/T_{\rm e}^2$, where $Z_{\rm eff}$ is assumed to be 3. The relationship between $\tau_{\rm E}$ and $\nu_{\rm eff}$ is summarized in Fig. 8. As a function of $\bar{n}_{\rm e}$, $au_{\rm E}$ exhibits significant scatter depending on $P_{\rm total}$. However, $au_{\rm E}$ dependence of $u_{\rm eff}$ exhibits improved consistency across different heating powers. As $\nu_{\rm eff}$ increases, $\tau_{\rm E}$ begins to saturate around $\nu_{\rm eff} \approx 0.1$ in the low $P_{\rm total}$ cases, whereas it continues to increase in the high P_{total} cases. A comparison between ECH and the higher ohmic heating discharges around 6×10^{18} m⁻³ shows that, although they appear to have different $\tau_{\rm E}$ at the same $\bar{n}_{\rm e}$, the increase in $\nu_{\rm eff}$ of the higher ohmic heating case is likely responsible for the improved confinement. It is known that, as $\nu_{\rm eff}$ increases, the dominant instability shifts from TEMs to the ion temperature gradient (ITG) mode, which leads to saturation in the linear increase of confinement time [17, 18]. Thus, it is qualitatively inferred that this transition occurs in the low $P_{\rm total}$ cases, whereas the TEM-dominated regime extends to higher $\bar{n}_{\rm e}$ ranges in the high $P_{\rm total}$ cases.

6. SUMMARY

The global energy confinement time $\tau_{\rm E}$ was evaluated for the JT-60SA plasma in the first operation phase with the line-averaged electron density $\bar{n}_{\rm e}=2.5$ – 6.5×10^{18} m $^{-3}$ and the electron temperature $T_{\rm e}=0.8$ –1.8 keV, yielding values of approximately 100–200 ms. The global energy confinement time decreased with increasing heating power, consistent with previous findings. On the other hand, its dependence on $\bar{n}_{\rm e}$ appeared nearly linear, which represented a stronger dependence than that predicted by the ITERL-96P(th) scaling. When the results were

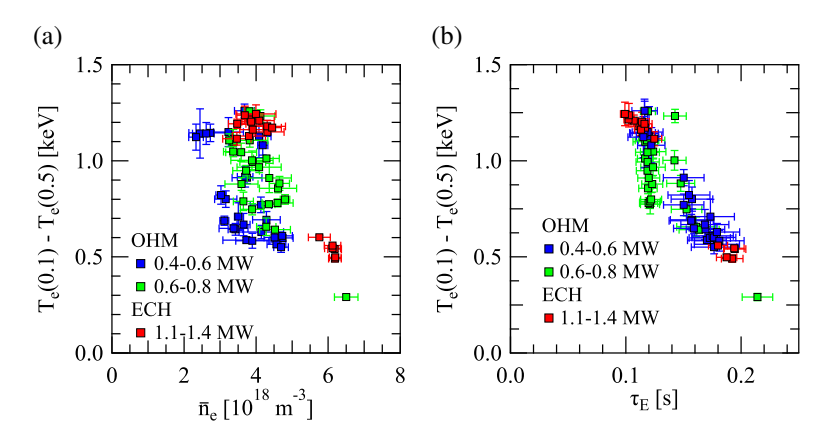


FIG. 7. (a) Relationship between \bar{n}_e and T_e gradient. Relationship between the T_e gradient and τ_E . The blue, green, and red squares are defined as in Fig. 5.

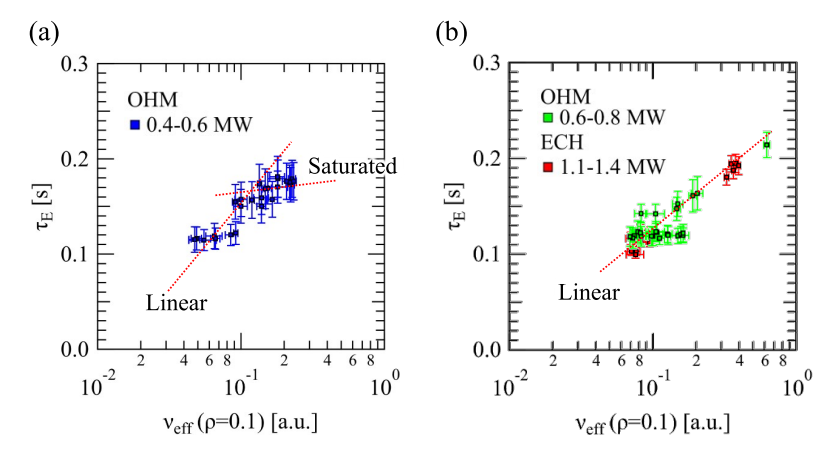


FIG. 8. Relationship between $\tau_{\rm E}$ and $\nu_{\rm eff}$ in (a) the lower $P_{\rm total}$ case, and (b) the higher $P_{\rm total}$ cases. The red dotted lines are eye guides. The blue, green, and red squares are defined as in Fig. 5.

overplotted on the ITERL-96P(th) scaling, the data at higher densities matched the scaling, while those at lower densities deviated by up to a factor of two below it.

Comparison with the neo-Alcator scaling revealed LOC–SOC-like behavior under lower ohmic heating conditions. However, in higher ohmic heating plasma and ECH plasma, only the linear dependence was observed. A decrease in $\tau_{\rm E}$ with an increase in the electron temperature $T_{\rm e}$ gradient was observed. These results are consistent with previous findings. This trend suggests that turbulent transport in these plasmas may remain dominated by trapped electron modes (TEMs) even at high densities. The dependence of $\tau_{\rm E}$ on the collisionality $\nu_{\rm eff}$ shows reduced scatter compared to $\bar{n}_{\rm e}$, indicating a common confinement behavior across heating powers. At low $P_{\rm total}$, $\tau_{\rm E}$ tends to saturate around $\nu_{\rm eff} \approx 0.1$, while in high $P_{\rm total}$ discharges, $\tau_{\rm E}$ continues to increase with $\nu_{\rm eff}$, implying a possible persistence of TEMs dominance at higher densities.

ACKNOWLEDGEMENTS

JT-60SA was jointly constructed and is jointly funded and exploited under the Broader Approach Agreement between Japan and EURATOM.

REFERENCES

- [1] M. Yoshida et al. "Overview of plasma operation and control studies in the first plasma campaign of JT-60SA". In: *Plasma Physics and Controlled Fusion* 67.6 (2025), p. 065010.
- [2] S.M. Kaye et al. "ITER L mode confinement database". In: Nuclear Fusion 37.9 (1997), p. 1303.
- [3] J. E. Rice et al. "Ohmic energy confinement saturation and core toroidal rotation reversal in Alcator C-Mod plasmas". In: *Physics of Plasmas* 19.5 (2012), p. 056106.

- [4] J.E. Rice et al. "Understanding LOC/SOC phenomenology in tokamaks". In: *Nuclear Fusion* 60.10 (2020), p. 105001.
- [5] Y.J. Shi et al. "Intrinsic rotation reversal, non-local transport, and turbulence transition in KSTAR L-mode plasmas". In: *Nuclear Fusion* 57.6 (2017), p. 066040.
- [6] Phase I Plasma Diagnostics. https://www.jt60sa.org/wp/phase-i-plasma-diagnostics/.
- [7] T. Kobayashi et al. "Development of two directional beam steering ECH/CD launcher for JT-60SA". In: *Fusion Engineering and Design* 146 (2019), pp. 1647–1651.
- [8] Y. Ohtani et al. "Real-time processing system of a two-color CO2 laser interferometer for density feedback control in JT-60SA". In: *Review of Scientific Instruments* 95.7 (2024), p. 073518.
- [9] H. Sasao et al. "Two-color CO2 laser long-distance interference measurements with long-time stabilization in JT-60SA". In: *Review of Scientific Instruments* 96.4 (2025), p. 043508.
- [10] R Sano et al. "Soft x-ray diagnostics system for electron temperature measurement in the integrated commissioning phase of JT-60SA". In: *Review of Scientific Instruments* 95.7 (2024), p. 073532.
- [11] T. Takeda and T. Tsunematsu. *A numerical code SELENE to calculate axisymmetric toroidal MHD equilibria*. Tech. rep. Japan Atomic Energy Research Institute, 1979.
- [12] S. Inoue et al. "Diamagnetic energy measurements and evaluation of poloidal beta and internal inductance during the first operational phase at JT-60SA". In: *Nuclear Fusion* 65.3 (2025), p. 036031.
- [13] ITER Physics Basis Editors et al. In: Nuclear Fusion 39.12 (1999), p. 2137.
- [14] Y. Ohtani et al. "Operational regime and confinement property of JT-60SA L-mode plasma in the first plasma operation phase". In: *Plasma Physics and Controlled Fusion* 67.5 (2025), p. 055042.
- [15] T. Yokoyama et al. "Characteristics of disruptions observed in the initial operation phase of JT-60SA". In: *Nuclear Fusion* 64.12 (2024), p. 126031.
- [16] K. Yanagihara and S. Kubo. "Broadening of electron cyclotron power deposition and driven current profiles caused by dissipative diffractive propagation". In: *Nuclear Fusion* 64.6 (2024), p. 066009.
- [17] C. Angioni et al. "Relationship between density peaking, particle thermodiffusion, Ohmic confinement, and microinstabilities in ASDEX Upgrade L-mode plasmas". In: *Physics of Plasmas* 12.4 (2005), p. 040701.
- [18] L. Qi et al. "Nonlinear gyrokinetic analysis of linear ohmic confinement to saturated ohmic confinement transition". In: *Nuclear Fusion* 60.3 (2020), p. 036009.